Nucleation and growth control for iron- and phosphorus-rich phases from a modified steelmaking waste slag

Juncheng Li[1),✉], *Guoxuan Li*[1)], *Feng Qiu*[1)], *Rong Wang*[1)], *Jinshan Liang*[1)], *Yi Zhong*[1)], *Dong Guan*[1)], *Jingwei Li*[2)], *Seetharaman Sridhar*[3)], *and Zushu Li*[4)]

1) School of Material Science and Engineering, Jiangsu University, Zhenjiang 212013, China

2) School of Materials Science and Engineering, Hefei University of Technology, Hefei 230009, China

3) Engineering of Matter, Transport and Energy, Arizona State University, Tempe, AZ 85287, USA

4) WMG, the University of Warwick, Coventry, CV4 7AL, UK

Abstract: Recovering the iron (Fe) and phosphorus (P) contained in steelmaking slags not only reduces the environmental burden caused by the accumulated slag, but also is the way to develop a circular economy and achieve sustainable development in the steel industry. We had previously found the possibility of recovering Fe and P resources, i.e., magnetite (Fe_3O_4) and calcium phosphate ($Ca_{10}P_6O_{25}$), contained in steelmaking slags by adjusting oxygen partial pressure and adding modifier B_2O_3. As a fundamental study for efficiently recovering Fe and P from steelmaking slag, in this study, the crystallization behavior of the $CaO–SiO_2–FeO–P_2O_5–B_2O_3$ melt has been observed *in situ*, using a confocal scanning laser microscope (CLSM). The kinetics of nucleation and growth of Fe- and P-rich phases have been calculated using a classical crystallization kinetic theory. During cooling, a Fe_3O_4 phase with faceted morphology was observed as the 1st precipitated phase in the isothermal interval of 1300–1150°C, while $Ca_{10}P_6O_{25}$, with rod-shaped morphology, was found to be the 2nd phase to precipitate in the interval of 1150–1000°C. The crystallization abilities of Fe_3O_4 and $Ca_{10}P_6O_{25}$ phases in the $CaO–SiO_2–FeO–P_2O_5–B_2O_3$ melt were quantified with the index of $(T_U − T_I)/T_I$ (where T_I represents the peak temperature of the nucleation rate and T_U stands for that of growth rate), and the crystallization ability of Fe_3O_4 was found to be larger than that of $Ca_{10}P_6O_{25}$ phase. The range of crystallization temperature for Fe_3O_4 and $Ca_{10}P_6O_{25}$ phases was optimized subsequently. The Fe_3O_4 and $Ca_{10}P_6O_{25}$ phases are the potential sources for ferrous feedstock and phosphate fertilizer, respectively.

Keywords: steelmaking slag; magnetite; calcium phosphate; nucleation; growth; kinetics

1. Introduction

Steelmaking slag generates in the converter steelmaking process, with its major components being CaO, SiO_2, and Fe_tO, as well as some valuable oxides, P_2O_5 and MnO for instance. Steelmaking slag is taken as a potential source for construction materials [1], adsorbents for wastewater treatment [2], ceramics [3–4], fertilizer [5], and ferrous feedstock in the iron and steelmaking process [6–8]. However, none of the above applications enable the sufficient utilization of steelmaking slags due to the technical and environmental obstacles, like volumetric expansion [9], disintegration [10], leaching of metals [11], and reverse of phosphorus to the hot metal [12]. Besides, the nonmagnetic valuable oxides, such as FeO and P_2O_5, in steelmaking slags have not been recovered. Thus, it would be of great significance to extract valuable elements from steelmaking slag. That is particularly true if considering the increasingly environmental burden and depletion of natural resources.

With the aim of recycling iron from metallurgical slags, several processes have been tried, such as the reduction of iron oxide to metallic Fe using C [13], CO [14], and H_2 [15] and the oxidation of FeO to Fe_3O_4 using air [16–18] and H_2O [19–21], followed by magnetic separation. However, the reduction methods suffer from some limitations, and reducing conditions are likely to promote phosphorus reversion to the hot metal [22]. The alternative approach of oxidation routes may enable the selective precipitation of Fe_3O_4 and subsequent separation of magnetite from the quenched slag by magnetic separation. Regarding phosphorus recycling from steelmaking slag, the following technologies have been adopted: flotation [23], magnetic separation [24], supergravity separation [25–27], reduction [28–30], leaching [31–33], and a three-stage continuous-selective process (selective enrichment–selective growth–selective separation) [34–36]. The above-mentioned technologies provide, to some degree, a better understanding of the phosphorus-containing phase formation to remove or extract phosphorus from steelmaking

---

🍃 Springer

slags, and the three-stage continuous selective process is regarded as the most promising process due to its high efficiency and low waste emission.

Based on the three-stage continuous selective process, Fe_3O_4 and $Ca_{10}P_6O_{25}$ phases were proved to be the optimized iron- and phosphorus-rich phases in the slags by controlling oxygen partial pressure and adding slag modifier of B_2O_3, which have been reported by our group [37]. In the three steps, the second step of optimizing conditions to facilitate the growth of Fe_3O_4 and $Ca_{10}P_6O_{25}$ phases in phosphorus-containing slags plays a key role in the subsequent technical step of selective separation, and therefore, the present work focuses on investigating nucleation and growth control for iron- and phosphorus-rich phases from synthesized steelmaking slag. Specifically, the crystallization behavior of the synthesized slag was determined by *in situ* observation via confocal scanning laser microscope (CLSM) and characterization through scanning electron microscopy with energy dispersive spectroscopy (SEM–EDS) and X-ray diffraction (XRD), while the kinetics of nucleation and growth of iron- and phosphorus-rich phases have been calculated by a classical crystallization kinetic model.

2. Experimental

2.1. Materials and sample preparation

A previous study [37] indicated that phosphorus (P) could be enriched in the form of calcium phosphate ($Ca_{10}P_6O_{25}$) phases through the addition of B_2O_3 to the steelmaking slags.

As a result, the synthesized slag system of CaO–SiO_2–FeO–P_2O_5–B_2O_3 was chosen to investigate the crystallization behaviors of the P-rich phase in this study. Table 1 presents the chemical composition of synthetic slags before and after melting. The synthetic slag was made in a platinum crucible by heating the mixture of reagent grades CaO, SiO_2, FeO, P_2O_5, and B_2O_3 at 1600°C in a vertical tube furnace for 2 h in an Ar atmosphere at the flow rate of 0.5 L/min, and then the synthesized slag was rapidly quenched into water. The equipped U-type thermocouple (Pt–30%Rh/Pt–6%Rh) serves to control the temperature of the vertical tube furnace, with an accuracy of ±3°C. The quenched slag sample was ground to slag powder, which is henceforth denoted as the pre-melted slag.

Table 1.   Chemical composition of the synthesized slag wt%

Sample	CaO	SiO$_2$	FeO	P$_2$O$_5$	B$_2$O$_3$
Designed	34.29	13.71	36	10	6
Measured	33.77	12.98	37.87	10.06	5.32

2.2. Experimental apparatus and procedure

To determine the crystallization temperature of different phases, CLSM (VL2000DX-SVF18SP from Yonekura MFG. Co. LTD, Japan) was applied to *in situ* observe the crystallization behavior. The thermal cycle employed in the isothermal experiment is shown in Fig. 1. Before the experiment, the process of evacuation of the CLSM chamber and the subsequent purging with argon gas was operated 3 times.
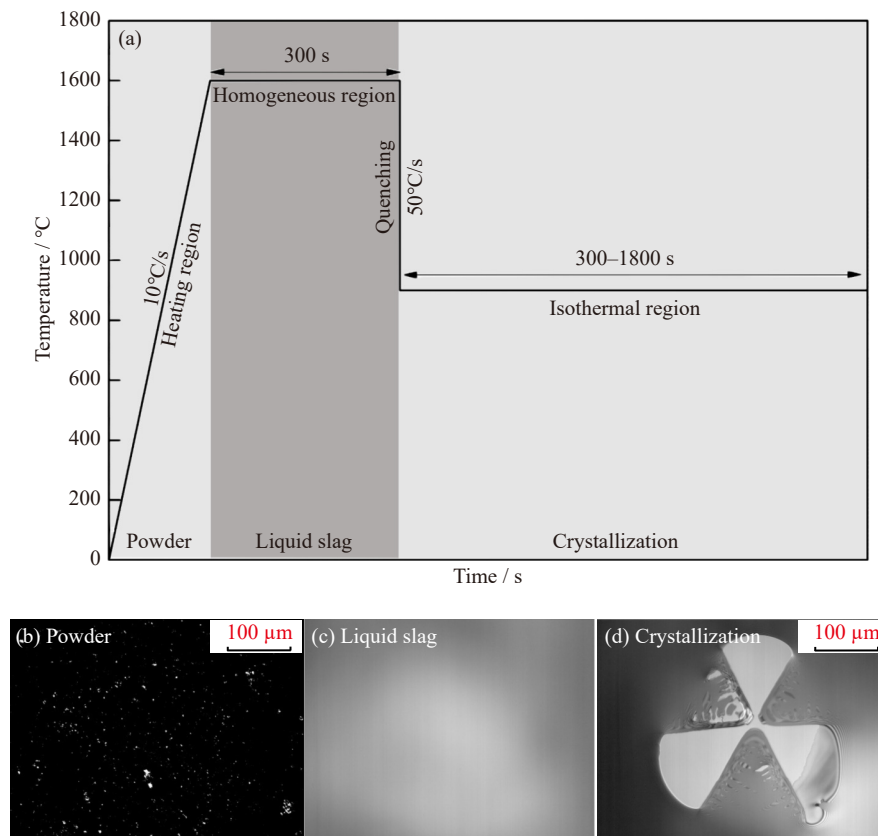

Fig. 1.   (a) Thermal cycle of isothermal experiment of the synthesized slag; (b) powder state; (c) liquid state; (d) crystallization state.

After that, a Pt crucible containing 0.2 g pre-melted slag was heated to 1600°C at the hot stage of CLSM under the Ar atmosphere, and that temperature would last for 5 min to homogenize the molten slag. Thereafter, the molten slag sample was quenched to a preset temperature that would be held for 5–30 min to construct the time-temperature-transformation (TTT) diagram by analyzing crystalline transformation with time and temperature. To identify the microstructure, element distribution, and mineral components, the samples were quenched at different temperatures and characterized by SEM-EDS (EVO 18 from Carl Zeiss AG) and by XRD (TTRIII from Rigaku Corporation).

3. Calculation

3.1. Analytical model

It has been broadly accepted that the crystallization of Fe_3O_4 and $Ca_{10}P_6O_{25}$ phases in the synthesized slag consists of two stages: nucleation and growth. Based on theories of nucleation and absolute rate, the classic crystallization kinetic concerning the nucleation and growth rate can be expressed by Eqs. (1) and (2), respectively [38–41].

$$I = N_0 kT \left(3\pi a^3 \eta\right)^{-1} \exp\left[-b\alpha^3\beta\left(\Delta T_r^2 T_r\right)^{-1}\right] \qquad (1)$$

$$U = f kT \left(3\pi a^2 \eta\right)^{-1} \left[1 - \exp\left(\frac{-\beta\Delta T_r}{T_r}\right)\right] \qquad (2)$$

where I and U refer to nucleation and growth rates; N_0, k, T, a, and η mean the number of molecules (or atoms) per unit volume, Boltzmann's constant, absolute temperature, lattice parameter of the crystal, and viscosity, respectively; b stands for a constant relating to the nucleus shape, which can be expressed in the form of $b = \dfrac{16\pi}{3}$ when assuming the crystals to be spherical in shape; T_r and ΔT_r are the reduced temperature and undercooling, which are defined as: $T_r = \dfrac{T}{T_m}$ and $\Delta T_r = 1 - T_r$, respectively; the fraction of acceptor sites in the crystal surface can be abbreviated to f in Eq. (3); α and β are the reduced crystal/liquid interfacial tension and reduced molar heat of fusion, which are defined as Eqs. (4) and (5), respectively.

$$f = \begin{cases} 1, & \Delta H_m < 2RT_m \\ 0.2\Delta T_r, & \Delta H_m > 4RT_m \end{cases} \qquad (3)$$

$$\alpha = \frac{\sigma\left(V^2 N_A\right)^{1/3}}{\Delta H_m} \qquad (4)$$

$$\beta = \frac{\Delta H_m}{RT_m} \qquad (5)$$

where σ, N_A, R, ΔH_m, T_m, and V refer to crystal/liquid interfacial tension, Avogadro's constant, gas constant, molar heat of fusion, the melting point of the crystal, and the molar volume of the crystal.

3.2. Determination of parameters

Our previous study [37] regarding the feasibility of separation and extraction of Fe- and P-rich phases from CaO–

SiO_2–FeO–P_2O_5–B_2O_3 slags has reported that Fe_3O_4 and $Ca_{10}P_6O_{25}$ phases were the target iron- and phosphorus-rich phases. As shown in Table 2, while the parameters of the structure are selected from databases of XRD standard patterns, the melting temperature is obtained from the reference book [42].

Table 2. Parameters of structure and melting point of Fe- and P-rich phases [42]

Phase	Lattice parameter, a / nm	Melting temperature / °C
Fe_3O_4	0.839	1870
$Ca_{10}P_6O_{25}$	0.943	2083

It is reported that the range from 1 to 10 occurs in most cases concerning the reduced molar heat of fusion (β) [39]. Only a few cases show the possibility of directly measuring the interfacial tension (α). Also, no specific theory can be found to predict α. Against this background, the current study cites the values of α and β (i.e., $\alpha = 1/3$ and $\beta = 1$) from the existing literature [43–44]. Notably, α and β share nearly the same value for crystalline phases in metallurgical melts, as evidenced by related literature on the application of the nucleation kinetic model [45–46], even though Fe_3O_4 and $Ca_{10}P_6O_{25}$ concerned are different materials with distinct properties in relation to the values of α and β. Therefore, α and β of Fe_3O_4 are identical to those of $Ca_{10}P_6O_{25}$ in this paper.

The viscosity of the synthesized slag was calculated by the Arrhenius equation as shown in Eq. (6).

$$\ln\eta = \ln A + \frac{B}{T} \qquad (6)$$

where A and B, constants in relation to temperature, can be expressed by Eqs. (7) and (8) that link the viscosity of slags to the structure through optical basicity [47].

$$\ln A = -232.69\Lambda^2 + 357.32\Lambda - 144.17 \qquad (7)$$

$$\ln\frac{B}{1000} = -1.77 + \frac{2.88}{\Lambda} \qquad (8)$$

where Λ is the optical basicity that can be calculated by Eq. (9),

$$\Lambda = \frac{\sum\chi_i n_i \Lambda_i}{\sum\chi_i n_i} \qquad (9)$$

where χ_i means mole fraction of each component in the synthesized slag, n_i represents the number of oxygen atoms of each component in the molecule (for example, $n = 1$ for CaO and $n = 2$ for SiO_2), and Λ_i refers to the optical basicity of slag components. The last parameter (Λ_i) used for calculation in this work is quoted from the literature [47–48] and presented in Table 3.

Table 3. Values of optical basicities (Λ_i) for the synthesized slag components [47–48]

CaO	SiO_2	FeO	P_2O_5	B_2O_3
1.0	0.48	1.0	0.4	0.42

4. Results and discussion

4.1. Visualization of crystallization and phase characterization

The crystallization evolutions of the synthesized slag at 1275, 1200, and 1100°C were imaged, as shown in Figs. 2–4, respectively. It can be seen that the nuclei of the primary phase formed when the temperature of molten slag decreased to 1275°C and held for 554 s (Fig. 2(a)). The number of crystal nuclei increased and the frame of the crystal gradually formed with the increasing holding time from 554 to 1164 s. Thereafter, the crystals continued to coarse, and then the amount of the liquid phase in the system decreased gradually (Fig. 2(b)–(f)). Finally, the crystal formed a faceted morphology, which is centered in the particle marked by the red dotted square (Fig. 2(f)). The crystals tended to have more prevalent faceted morphology when the degree of supercooling was lower, which generally agrees with the morphology of molten CaO–SiO$_2$–FeO–MnO slags as reported in our previous investigation [20].

Interestingly, the crystal nuclei, looking like gravel, were observed to form when the molten slag was quenched to 1200°C and remained the same for 98 s (Fig. 3(a)). With the holding time increasing from 98 to 137 s, the morphology of crystals transformed from gravel shape into two petal-like crystals (Fig. 3(b)), then into a boomerang-shaped morpho-

logy (Fig. 3(c)), and subsequently into a crab-like pincer shape (Fig. 3(d)). Finally, crystals, with well-balanced and symmetrical clover patterns, started to form at 145 s (Fig. 3(e)), accompanying the precipitation of some new crystal nuclei at the gap of clover leaves at 162 s (Fig. 3(f)). In summary, with the holding time increasing from 98 to 162 s, nucleation and growth of crystal appeared a dynamic process, which is a transition from a non-equilibrium state to an equilibrium state and from asymmetric patterns to symmetric ones.

In comparison, a rod-shaped morphology appeared when the temperature of molten slag reached 1100°C and held for 61 s (Fig. 4(a)). As indicated in Fig. 4(b), the growth of rod-shaped crystals towards the center of the sample may suggest heterogeneous nucleation of the molten slag. With the holding time increasing from 357 to 1084 s, while the crystal nucleus increasingly grew and coarsened, the liquid slag began to lessen (Fig. 4(c)–(f)).

The different phase precipitation sequence at different isothermal temperatures for the CaO–SiO$_2$–FeO–P$_2$O$_5$–B$_2$O$_3$ melt could be owing to such factors as undercooling [49], slag composition [50], and enthalpy of mixing [51] that would be investigated in a separate paper.

Fig. 5 compares the morphology of the crystalline observed by CLSM with that characterized by SEM for the slag holding at 1100°C for 1084 s. It should be pointed out that
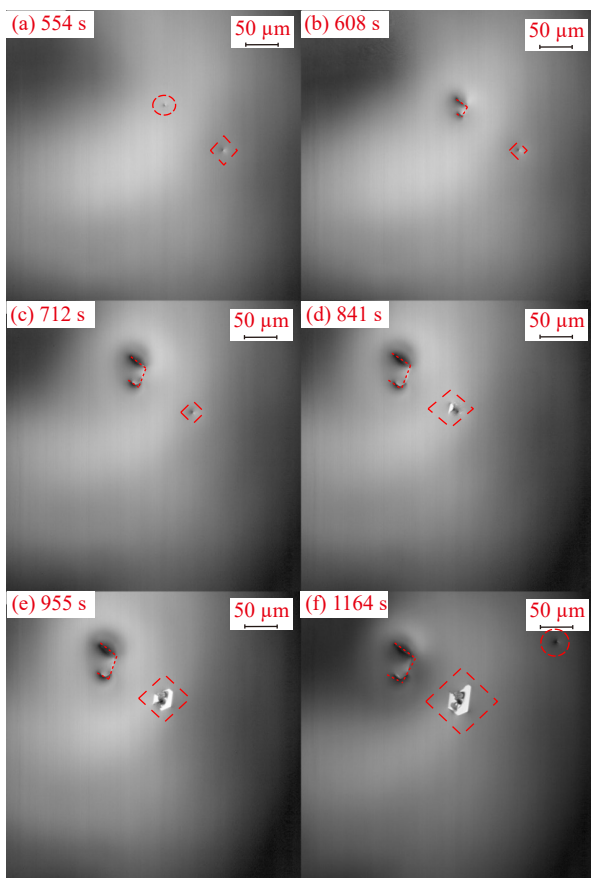

Fig. 2. Evolution of crystal morphologies of the synthesized slag at 1275°C for (a) 554 s, (b) 608 s, (c) 712 s, (d) 841 s, (e) 955 s, and (f) 1164 s, respectively.
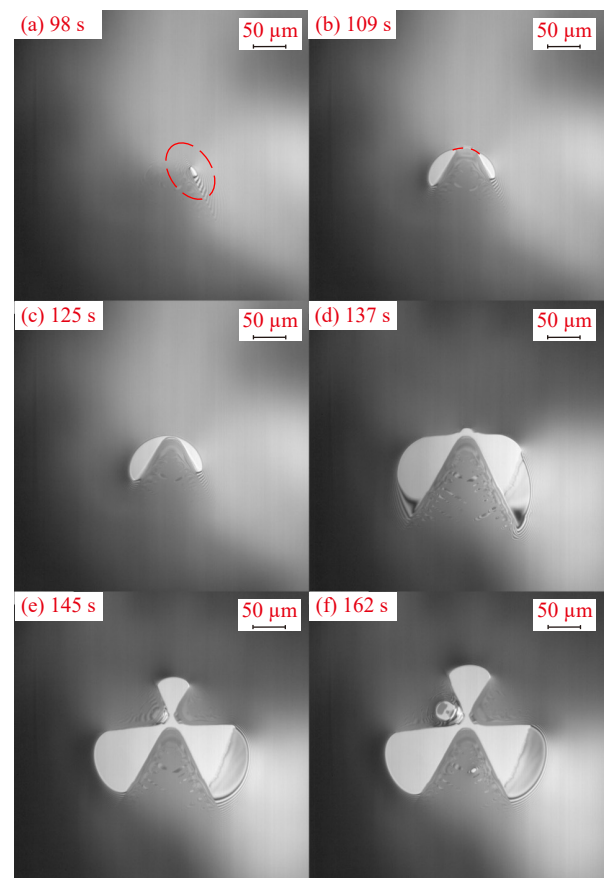

Fig. 3. Evolution of crystal morphologies of the synthesized slag at 1200°C for (a) 98 s, (b) 109 s, (c) 125 s, (d) 137 s, (e) 145 s, (f) 162 s, respectively.
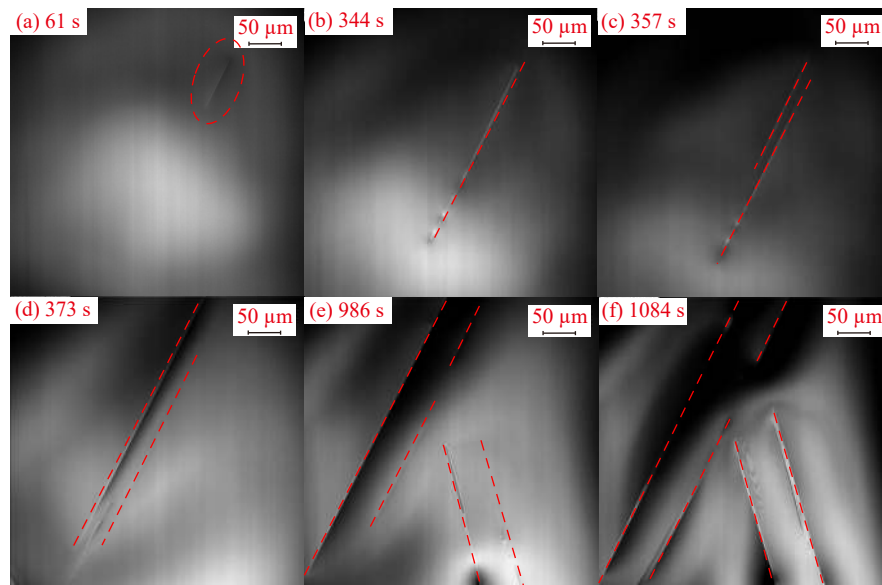
Fig. 4.   Evolution of crystal morphologies of the synthesized slag at 1100°C for (a) 61 s, (b) 344 s, (c) 357 s, (d) 373 s, (e) 986 s, (f) 1084 s, respectively.
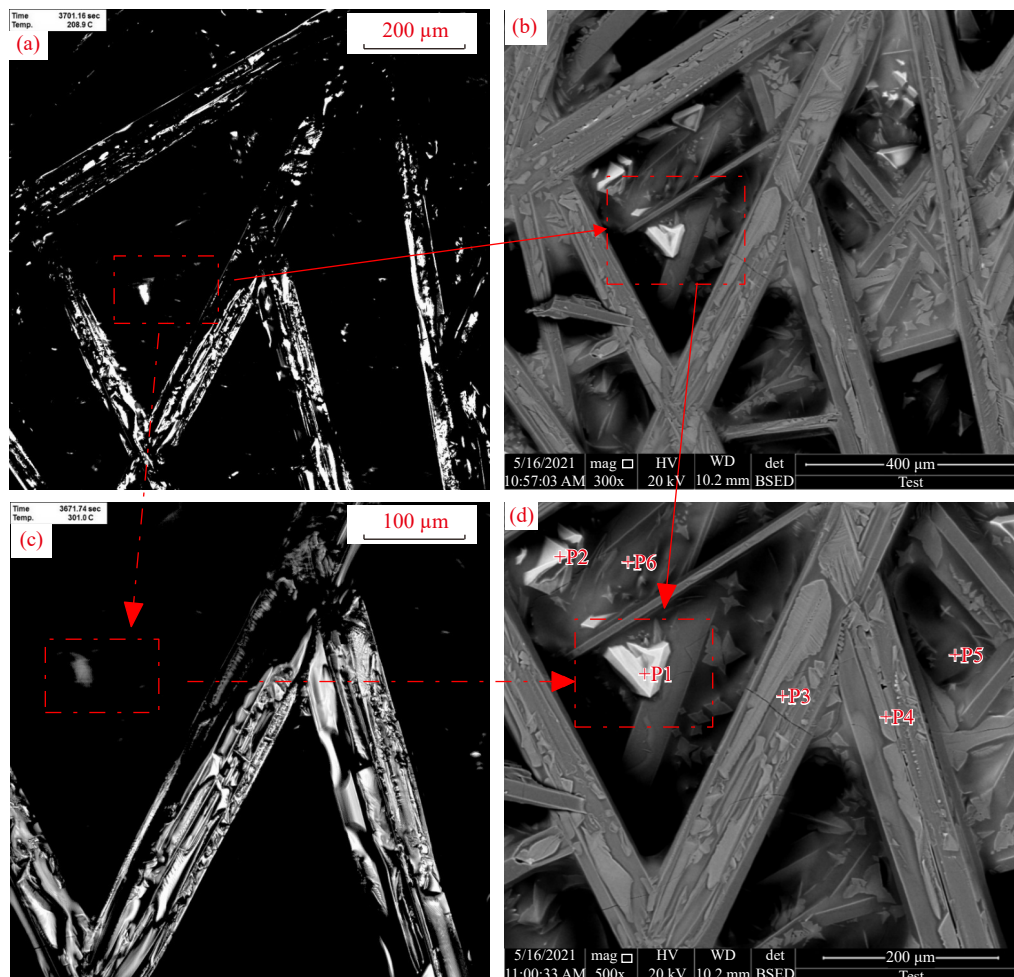

Fig. 5.   Crystal morphology of different phases in the slag at 1100°C: (a) 275× CLSM image; (b) 300× SEM image; (c) 550× CLSM image; (d) 500× SEM image.

these white hexagonally faceted crystals (P1 and P2) were surrounded by the lath-shaped phase (P3 and P4) and slag matrix (P5 and P6), which implies an early crystallization of faceted crystals, rather than lath-shaped phase and slag mat-rix. As shown in Fig. 6, iron and phosphorus were mainly concentrated in the faceted and lath-shaped phases respect-ively. Moreover, the slag matrix was mainly composed of Ca and Si. Accordingly, the measured chemistry of the above-
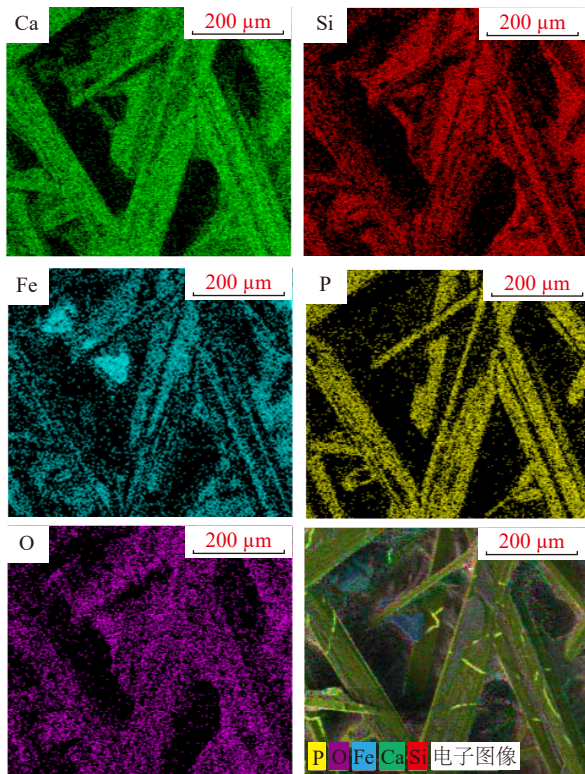
Fig. 6.   EDS map scanning of synthesized slag quenched from 1100°C.

mentioned three phases was close to $Fe_3O_{3.9}$ (or $Fe_3O_{4.2}$), $Ca_2PO_{4.8}$ (or Ca_2PO_4), and $CaFe_{0.3}Si_{0.7}O_{2.1}$ (or $CaFe_{0.3}Si_{0.8}O_{2.1}$) respectively, as presented in Table 4.

Fig. 7 shows the TTT diagram of the synthesized slag. As can be seen, the TTT diagram presented a double C shape and was divided into two regions above and below 1150°C. This may suggest that there were two different nucleation events in the crystallization process of the synthesized slag, and that the crystal morphology drastically changed around 1150°C. The representative slags from 1200, 1150, and 1100°C were analyzed by drawing on XRD with a view to identifying the crystalline phases formed in the two distinct regions. Fig. 8 describes the XRD patterns of the representative slags. More specifically, dramatic changes occurred in the precipitated phases as a function of temperature. Fe_3O_4 dominated the upper C section featuring a relatively higher temperature from 1300 to 1150°C. As for the lower C section characterizing isothermal temperature to below 1150°C, $Ca_{10}P_6O_{25}$ started to precipitate, and Fe_3O_4 and $Ca_{10}P_6O_{25}$

were the main crystalline phases in the slag with the temperature decreasing from 1150 to 1000°C.

In addition, it is clear that the crystallization becomes easier as the temperature decreases from 1300 to 1200°C and from 1150 to 1100°C (Fig. 7), as suggested by the shorter incubation time from 721 to 98 s and from 216 to 61 s respectively. It could be ascribed to the insufficient supercooling degree for the crystallization of slag [52]. However, it seems that the crystallization tends to be a little bit difficult with the temperature decreasing from 1200 to 1150°C and from 1100 to 1000°C. The results could be attributed to the difficult movement and nucleation of the ions in the melt caused by lower temperature. Hence, temperature plays a key role in controlling the crystallization of molten slag on the basis of TTT (Fig. 7) and XRD (Fig. 8). In order to recover iron and phosphorus in the form of Fe_3O_4 and $Ca_{10}P_6O_{25}$ phases from synthesized slag, it is necessary to investigate the optimum temperature range for the crystallization of Fe_3O_4 and $Ca_{10}P_6O_{25}$ phases, which will be discussed in Section 4.2.

4.2. Nucleation and growth kinetics of Fe- and P-rich phases

Targeting the recovery of iron and phosphorus from the synthesized slag, the kinetics for nucleation and growth of Fe- and P-rich phases is key, since the proportion and grain size of those phases significantly affect the upcoming iron and phosphorus separation process. Drawing on the kinetic model in the current study, the nucleation and growth rates of Fe_3O_4 and $Ca_{10}P_6O_{25}$ phases were calculated, as shown in Figs. 9 and 10. In general, a peak appeared in those two rates for Fe_3O_4 and $Ca_{10}P_6O_{25}$ phases, which is in line with the fact that nucleation and crystal growth rates are affected by the degree of supercooling and diffusive mass transfer in the synthesized slag, two contrary factors. Taking the $Ca_{10}P_6O_{25}$ phase as an example, the nucleation rate first increased to the maximum of 0.5×10^{26} $m^{-3} \cdot s^{-1}$ at 876°C, followed by a decline. The same situation occurred in growth rate with a maximum of 5.57×10^{-4} $m \cdot s^{-1}$ at 996°C.

The ability of a substance to form an amorphous/crystal solid has been examined in Wu *et al.*'s work [53]. To put it in a more specific way, the crystallization abilities of precipitated phases can be expressed by $(T_U - T_I)/T_I$, in which T_I means the peak temperature of nucleation rate and T_U refers to that of the growth rate. A larger value of $(T_U - T_I)/T_I$ indicates a better ability to form an amorphous solid. Otherwise, a

Table 4.   EDS results of the slag quenched at 1100°C, corresponding to Fig. 5(d)

Phase	Ca / wt%	Si / wt%	O / wt%	P / wt%	Fe / wt%	Potential formula
P1	1.19	—	26.71	—	72.1	$Fe_3O_{3.9}$
P2	2.88	0.53	27.64	—	68.95	$Fe_3O_{4.2}$
P3	41.87	1.25	40.01	16.87	—	$Ca_2PO_{4.8}$
P4	44.28	2.43	35.74	17.55	—	Ca_2PO_4
P5	36.28	17.83	31.13	0.55	14.21	$CaFe_{0.3}Si_{0.7}O_{2.1}$
P6	35.03	18.53	29.59	—	16.85	$CaFe_{0.3}Si_{0.8}O_{2.1}$

Note: — indicates that the elements involved have not been detected due to their relatively tiny amount in the phase area; low X-ray energy boron has not been listed in this table.
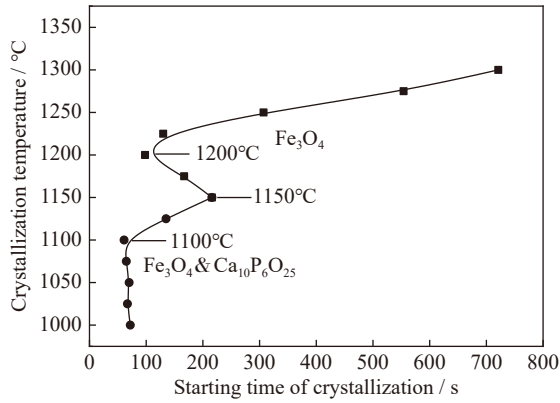
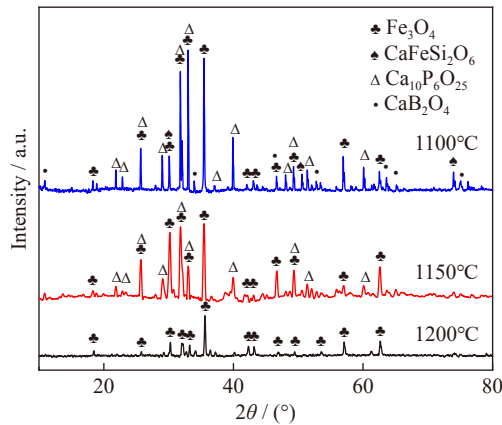**Fig. 7.   TTT diagram of synthesized slag.**

Fig. 8.   XRD patterns of the slags quenched from 1200, 1150, and 1100°C, respectively.

Fig. 9.   Nucleation rate of Fe_3O_4 and $Ca_{10}P_6O_{25}$ phases in synthesized slag.

Fig. 10.   Growth rate of Fe_3O_4 and $Ca_{10}P_6O_{25}$ phases in synthesized slag.

Table 5.   Crystallization abilities of Fe_3O_4 and $Ca_{10}P_6O_{25}$ phases in the synthesized slag

Phase	T_I / °C	T_U / °C	$(T_U - T_I)/T_I$
Fe_3O_4	1083	1140	0.0526
$Ca_{10}P_6O_{25}$	876	996	0.1370

crystal solid would preferentially form. The peak temperatures derived from Figs. 9 and 10 are presented in Table 5, and the crystallization abilities of Fe_3O_4 and $Ca_{10}P_6O_{25}$ phases in synthesized slag were obtained as well. It is evident that $(T_U - T_I)/T_I$ of the $Ca_{10}P_6O_{25}$ phase shows a relatively small value. What is more, Fe_3O_4 suggests a smaller value than $Ca_{10}P_6O_{25}$, indicating the larger crystallization ability of Fe_3O_4 than that of the $Ca_{10}P_6O_{25}$ phase in the synthesized slag.

However, the different peak temperatures of the nucleation rate and growth rate between Fe_3O_4 and $Ca_{10}P_6O_{25}$ phases make it hard to decide an accurate optimum temperature range for the precipitated phases in the synthesized slag. Fortunately, Johnson and Mehl [54] derived expressions as shown in Eq. (10), which demonstrates the relationship between transformed fraction φ and the following three factors: nucleation rate I, growth rate U, and time t.

$$\varphi = 1 - \exp\left(-\frac{\pi}{3}IU^3t^4\right) \tag{10}$$

herein, $\frac{\pi}{3}IU^3$ is termed crystallization rate r as presented in Eq. (11),

$$r = \frac{\pi}{3}IU^3 \tag{11}$$

Assuming Fe and P merely exist in Fe_3O_4 and $Ca_{10}P_6O_{25}$ phases in the synthesized slag, the total crystallization rate r_{Total} can be defined by applying Eq. (12),
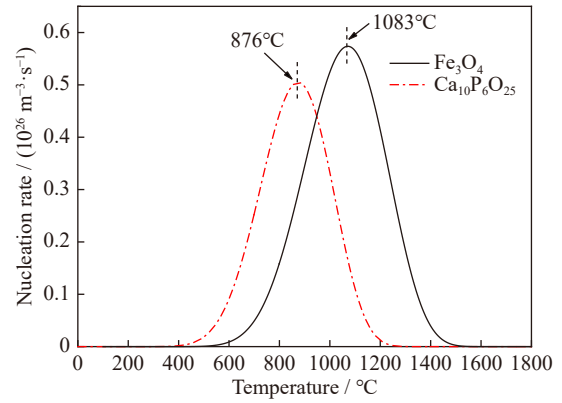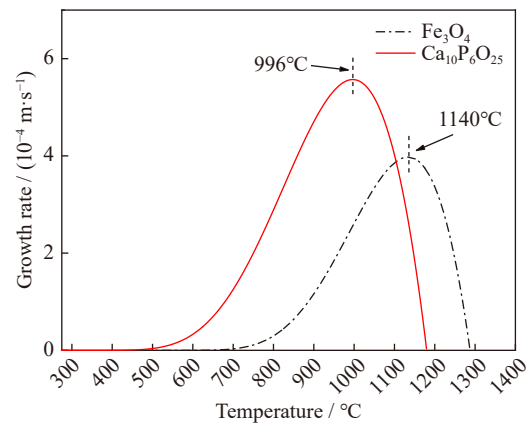
$$r_{Total} = \sum_{i=1}^{2} w_i r_i \tag{12}$$

where w_i and r_i refer to the mass fractions and crystallization rates of the Fe_3O_4 and $Ca_{10}P_6O_{25}$ phases in the synthesized slag. In this study, the mass fraction of the Fe_3O_4 and $Ca_{10}P_6O_{25}$ are 0.636 and 0.364.

Fig. 11 describes the crystallization rates of Fe_3O_4 and $Ca_{10}P_6O_{25}$ phases. In comparison with the $Ca_{10}P_6O_{25}$ phase, Fe_3O_4 exerted a remarkable effect on the total crystallization rate, which agrees well with the crystallization abilities of Fe_3O_4 and $Ca_{10}P_6O_{25}$ phases estimated by $(T_U - T_I)/T_I$ in Table 5. Notably, Fig. 11 suggests that the precipitation of Fe_3O_4 is before that of $Ca_{10}P_6O_{25}$ in the synthesized slag, which is in accordance with the precipitation sequence of precipitated phases observed by CLSM in Figs. 2–4. The corresponding temperature to the maximum total crystallization rate was 1055°C in Fig. 11, and the optimum temperature range is thus defined as (1055 ± 25)°C (i.e., 1080–1030°C) in relation to the crystallization of Fe_3O_4 and $Ca_{10}P_6O_{25}$ phases.

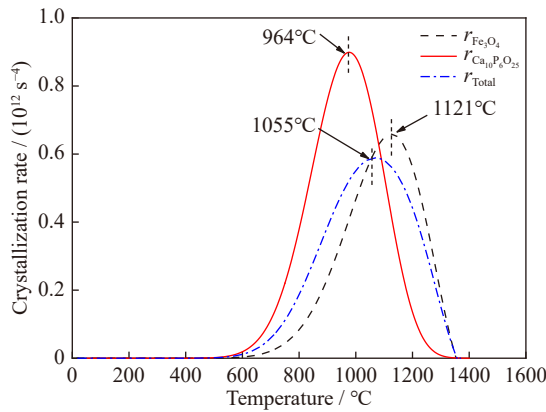**Fig. 11.   Crystallization rates of Fe₃O₄ and Ca₁₀P₆O₂₅ phases in synthesized slag.**

Based on the investigation results in the current study, an optimized heat treatment process for the synthesized slag as illustrated in Fig. 12 has been proposed to develop Fe_3O_4 and $Ca_{10}P_6O_{25}$ phases with a larger size. The cooling rate is symbolized by θ in Fig. 12, and the corresponding temperatures for the maximum crystallization rates of Fe_3O_4 and $Ca_{10}P_6O_{25}$

phases are 1121 and 964°C. To facilitate the subsequent selective separation of Fe_3O_4 and $Ca_{10}P_6O_{25}$ from the synthesized slag, the larger sizes of Fe_3O_4 and $Ca_{10}P_6O_{25}$ are preferred since the extraction efficiency of Fe and P strongly depends on crystal size. Relatively small cooling rates of θ_2 and θ_3 should be given in an attempt to provide enough time for the nucleation and growth of Fe_3O_4 and $Ca_{10}P_6O_{25}$. On the contrary, the precipitation of silicate phases should be restricted by setting θ_4 at a large value. For the simple industrial application of extracting iron and phosphorus contained in steelmaking slag, B_2O_3 should be added into the molten steelmaking slag during the slag tapping process to facilitate the precipitation of Fe_3O_4 and $Ca_{10}P_6O_{25}$ phases. In order for Fe_3O_4 and $Ca_{10}P_6O_{25}$ to grow, slag from the converter should be held in slag ladles for several heats till 964°C. Thereafter, the slag concerned can be water quenched with a view to restricting the precipitation of silicate phases. Finally, the larger size of Fe_3O_4 and $Ca_{10}P_6O_{25}$ could be selectively separated by combining magnetic separation with flotation, as reported in our previous paper [37].

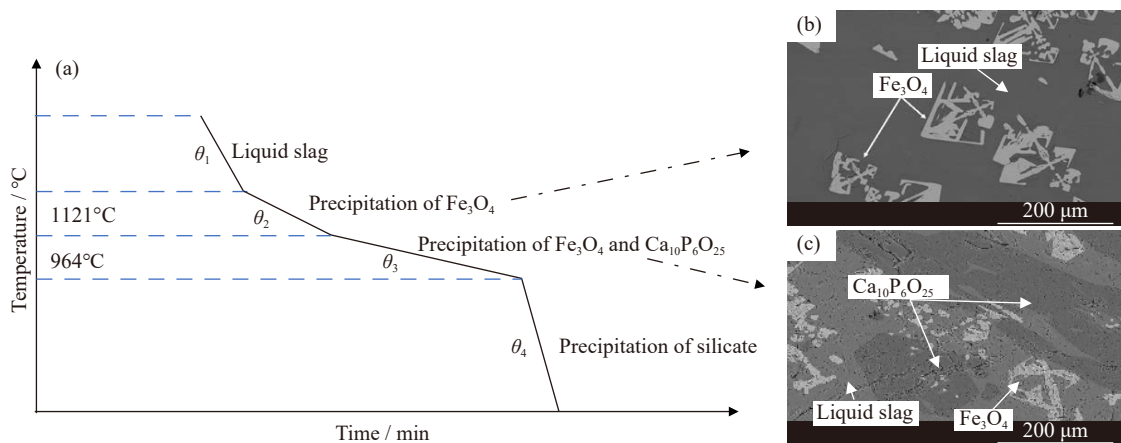**Fig. 12.   (a) Schematic diagram of suitable heat treatment condition; (b) precipitation of Fe₃O₄ phase; (c) precipitation of Fe₃O₄ and Ca₁₀P₆O₂₅ phases.**

5. Conclusions

In this study, the crystallization behavior of the CaO–SiO₂–FeO–P₂O₅–B₂O₃ melt has been *in situ* observed using a confocal scanning laser microscope. The kinetics of nucleation and growth of Fe_3O_4 and $Ca_{10}P_6O_{25}$ phases have been calculated by a classical crystallization kinetic model. The main conclusions are as follows.

(1) Fe_3O_4 with faceted morphology was found as the 1st precipitate phase in the isothermal interval of 1300–1150°C, while $Ca_{10}P_6O_{25}$ with rod-shaped morphology as the 2nd precipitate phase was observed in the isothermal interval of 1150–1000°C. Accordingly, the TTT curve has two C shapes, Fe_3O_4 and $Ca_{10}P_6O_{25}$ have different precipitation temperature ranges, with the phase transition temperature at 1150°C.

(2) The crystallization abilities of Fe_3O_4 and $Ca_{10}P_6O_{25}$ in the synthesized slag were evaluated with the index of $(T_U -$

$T_I)/T_I$, and the crystallization ability of Fe_3O_4 is larger than that of the $Ca_{10}P_6O_{25}$ phase. The optimum temperature range for the crystallization of Fe_3O_4 and $Ca_{10}P_6O_{25}$ phases is obtained as (1055 ± 25)°C, i.e., 1080–1030°C by both theoretical calculation and experiment.

Conflict of Interest

The authors declare no potential conflict of interest.

References

[1] I. Sosa, C. Thomas, J.A. Polanco, J. Setién, and P. Tamayo, High performance self-compacting concrete with electric arc furnace slag aggregate and cupola slag powder, *Appl. Sci.*, 10(2020), No. 3, art. No. 773.

[2] G.M.P. Kumara and K. Kawamoto, Steel slag and autoclaved aerated concrete grains as low-cost adsorbents to remove Cd^{2+} and Pb^{2+} in wastewater: Effects of mixing proportions of grains and liquid-to-solid ratio, *Sustainability*, 13(2021), No. 18, art. No. 10321.

[3] Q.S. Wu and Z.C. Huang, Preparation and performance of lightweight porous ceramics using metallurgical steel slag, *Ceram. Int.*, 47(2021), No. 18, p. 25169.

[4] Z.J. Tang, J. Liang, W.H. Jiang, *et al.*, Preparation of high strength foam ceramics from sand shale and steel slag, *Ceram. Int.*, 46(2020), No. 7, p. 9256.

[5] L. Lin, Y.Q. Liu, J.G. Zhi, *et al.*, Influence of slag temperature on phosphorus enrichment in P-bearing steelmaking slag, *Ironmaking Steelmaking*, 48(2021), No. 3, p. 334.

[6] H. Matsuura, X. Yang, G.Q. Li, Z.F. Yuan, and F. Tsukihashi, Recycling of ironmaking and steelmaking slags in Japan and China, *Int. J. Miner. Metall. Mater.*, 29(2022), No. 4, p. 739.

[7] S. Seetharaman, L.J. Wang, and H.J. Wang, Slags containing transition metal (chromium and vanadium) oxides—Conversion from ticking bombs to valuable resources: Collaborative studies between KTH and USTB, *Int. J. Miner. Metall. Mater.*, 29(2022), No. 4, p. 750.

[8] J.H. Zhao, P.Y. Yan, and D.M. Wang, Research on mineral characteristics of converter steel slag and its comprehensive utilization of internal and external recycle, *J. Cleaner Prod.*, 156(2017), p. 50.

[9] L.M. Juckes, The volume stability of modern steelmaking slags, *Trans. Inst. Min. Metall. Sect. C*, 112(2003), No. 3, p. 177.

[10] F. Engström, D. Adolfsson, Q. Yang, C. Samuelsson, and B. Björkman, Crystallization behaviour of some steelmaking slags, *Steel Res. Int.*, 81(2010), No. 5, p. 362.

[11] J.F.P. Gomes and C.G. Pinto, Leaching of heavy metals from steelmaking slags, *Rev. Metal.*, 42(2006), No. 6, p. 409.

[12] L.J. Chen, Y. Wan, X.J. Xia, J. Li, Y.D. Yang, and A. Mclean, Dephosphorisation of hot metal containing moderate amounts of chromium with $CaO–FeO_x–Cr_2O_3–CaF_2$ slag, *Ironmaking Steelmaking*, 48(2021), No. 7, p. 868.

[13] D.J. Min, J.W. Han, and W.S. Chung, A study of the reduction rate of FeO in slag by solid carbon, *Metall. Mater. Trans. B*, 30(1999), No. 2, p. 215.

[14] D.Q. Fan, M. Elzohiery, Y. Mohassab, and H.Y. Sohn, The kinetics of carbon monoxide reduction of magnetite concentrate particles through CFD modelling, *Ironmaking Steelmaking*, 48(2021), No. 7, p. 769.

[15] A. Heidari, N. Niknahad, M. Iljana, and T. Fabritius, A review on the kinetics of iron ore reduction by hydrogen, *Materials*, 14(2021), No. 24, art. No. 7540.

[16] A. Semykina, J. Nakano, S. Sridhar, V. Shatokha, and S. Seetharaman, Confocal microscopic studies on evolution of crystals during oxidation of the $FeO–CaO–SiO_2–MnO$ slags, *Metall. Mater. Trans. B*, 41(2010), No. 5, p. 940.

[17] A. Semykina, The kinetics of oxidation of liquid $FeO–MnO–CaO–SiO_2$ slags in air, *Metall. Mater. Trans. B*, 43(2012), No. 1, p. 56.

[18] A. Semykina, J. Nakano, S. Sridhar, V. Shatokha, and S. Seetharaman, Confocal scanning laser microscopy studies of crystal growth during oxidation of a liquid $FeO–CaO–SiO_2$ slag, *Metall. Mater. Trans. B*, 42(2011), No. 3, p. 471.

[19] W.J. Duan, Q.B. Yu, T.W. Wu, F. Yang, and Q. Qin, The steam gasification of coal with molten blast furnace slag as heat carri-er and catalyst: Kinetic study, *Int. J. Hydrogen Energy*, 41(2016), No. 42, p. 18995.

[20] J.C. Li, D. Bhattacharjee, X.J. Hu, D.W. Zhang, S. Sridhar, and Z.S. Li, Crystallization behavior of liquid $CaO–SiO_2–FeO–MnO$ slag in relation to its reaction with moisture, *Metall. Mater. Trans. B*, 50(2019), No. 4, p. 1931.

[21] J.C. Li, D. Bhattacharjee, X.J. Hu, D.W. Zhang, S. Sridhar, and Z.S. Li, Effects of slag composition on H_2 generation and magnetic precipitation from molten steelmaking slag–steam reaction, *Metall. Mater. Trans. B*, 50(2019), No. 2, p. 1023.

[22] B. Malvoisin, F. Brunet, J. Carlut, *et al.*, High-purity hydrogen gas from the reaction between BOF steel slag and water in the 473–673 K range, *Int. J. Hydrogen Energy*, 38(2013), No. 18, p. 7382.

[23] W.Z. Wang, B. Liang, and J.R. Zhang, Experimental study on low temperature flotation recovery of apatite from a magnetic tailings, *Appl. Mech. Mater.*, 522-524(2014), p. 1501.

[24] K. Matsubae-Yokoyama, H. Kubo, and T. Nagasaka, Recycling effects of residual slag after magnetic separation for phosphorus recovery from hot metal dephosphorization slag, *ISIJ Int.*, 50(2010), No. 1, p. 65.

[25] C. Li, J.T. Gao, F.Q. Wang, and Z.C. Guo, Enriching Fe-bearing and P-bearing phases from steelmaking slag melt by super gravity, *Ironmaking Steelmaking*, 45(2018), No. 1, p. 44.

[26] C. Li, J.T. Gao, and Z.C. Guo, Separation of phosphorus- and iron-enriched phase from $CaO–SiO_2–FeO–MgO–P_2O_5$ melt with super gravity, *Metall. Mater. Trans. B*, 47(2016), No. 3, p. 1516.

[27] C. Li, J.T. Gao, and Z.C. Guo, Isothermal enrichment of P-concentrating phase from $CaO–SiO_2–FeO–MgO–P_2O_5$ melt with super gravity, *ISIJ Int.*, 56(2016), No. 5, p. 759.

[28] Y.Y. Zhang, Q.G. Xue, G. Wang, and J.S. Wang, Gasification and migration of phosphorus from high-phosphorus iron ore during carbothermal reduction, *ISIJ Int.*, 58(2018), No. 12, p. 2219.

[29] M. Sugata, T. Sugiyama, and S.I. Kondo, Reduction of iron oxide contained in molten slags with solid carbon, *ISIJ Int.*, 14(1974), No. 2, p. 88.

[30] S. Takeuchi, N. Sano, and Y. Matsushita, Separate recovery of iron and phosphorus from BOF slags by using Fe–Si alloys, *Tetsu-to-Hagane*, 66(1980), No. 14, p. 2050.

[31] C.M. Du, X. Gao, S. Ueda, and S.Y. Kitamura, Separation and recovery of phosphorus from steelmaking slag via a selective leaching-chemical precipitation process, *Hydrometallurgy*, 189(2019), art. No. 105109.

[32] T. Teratoko, N. Maruoka, H. Shibata, and S.Y. Kitamura, Dissolution behavior of dicalcium silicate and tricalcium phosphate solid solution and other phases of steelmaking slag in an aqueous solution, *High Temp. Mater. Process.*, 31(2012), No. 4-5, p. 329.

[33] M. Numata, N. Maruoka, S.J. Kim, and S.Y. Kitamura, Fundamental experiment to extract phosphorous selectively from steelmaking slag by leaching, *ISIJ Int.*, 54(2014), No. 8, p. 1983.

[34] H.M. Xue, J. Li, Y.J. Xia, Y. Wan, L.J. Chen, and C.J. Lv, Mechanism of phosphorus enrichment in dephosphorization slag produced using the technology of integrating dephosphorization and decarburization, *Metals*, 11(2021), No. 2, art. No. 216.

[35] J.M. Gonzalez, C.J. Penn, and S.J. Livingston, Utilization of steel slag in blind inlets for dissolved phosphorus removal, *Water*, 12(2020), No. 6, art. No. 1593.

[36] G.F. Ye, J. Yang, R.H. Zhang, W.K. Yang, and H. Sun, Behavior of phosphorus enrichment in dephosphorization slag at low temperature and low basicity, *Int. J. Miner. Metall. Mater.*, 28(2021), No. 1, p. 66.

[37] G.X. Li, J.S. Liang, J. Long, *et al.*, A novel process for separa-

tion of magnetite and phosphorous phases from a CaO–SiO$_2$–FeO–P$_2$O$_5$ slag, *ISIJ Int.*, 62(2022), No. 7, p. 1556.

[38] D. Turnbull, Formation of crystal nuclei in liquid metals, *J. Appl. Phys.*, 21(1950), No. 10, p. 1022.

[39] D. Turnbull, Under what conditions can a glass be formed? *Contemp. Phys.*, 10(1969), No. 5, p. 473.

[40] J.C. Fisher, J.H. Hollomon, and D. Turnbull, Rate of nucleation of solid particles in a subcooled liquid, *Science*, 109(1949), No. 2825, p. 168.

[41] D.R. Uhlmann, A kinetic treatment of glass formation, *J. Non-Cryst. Solids*, 7(1972), No. 4, p. 337.

[42] I. Barin, *Thermochemical Data of Pure Substances*, 3rd ed., VCH Verlagsgesellschaft mbH, Weinheim, 1995, p. 478.

[43] B. Li and Z.T. Sui, Glass crystallization kinetics of CaO–MgO–Fe$_2$O$_3$–Al$_2$O$_3$–SiO$_2$ slags, *Chin. J. Mater. Res.*, 13(1999), No. 4, p. 412.

[44] P.X. Zhang, Z.T. Sui, D.M. Luo, and R.J. Ma, Study on crystallization kinetics of component containing boron in MgO–B$_2$O$_3$–SiO$_2$–Al$_2$O$_3$–CaO slag, *Chin. J. Mater. Res.*, 9(1995), No. 1, p. 66.

[45] X. Zhang, B. Xie, J. Diao, and X.J. Li, Nucleation and growth kinetics of spinel crystals in vanadium slag, *Ironmaking Steelmaking*, 39(2012), No. 2, p. 147.

[46] X. Lan, J.T. Gao, Z.W. Wang, and Z.C. Guo, Viscosity of RE-bearing slag systems and kinetics of nucleation and growth for RE-phases, *Ceram. Int.*, 48(2022), No. 9, p. 13304.

[47] K.C. Mills and S. Sridhar, Viscosities of ironmaking and steelmaking slags, *Ironmaking Steelmaking*, 26(1999), No. 4, p. 262.

[48] E. Bordes-Richard, Multicomponent oxides in selective oxidation of alkanes theoretical acidity versus selectivity, *Top. Catal.*, 50(2008), p. 82.

[49] X.F. Lei and X.X. Xue, Preparation, characterization and photocatalytic activity of sulfuric acid-modified titanium-bearing blast furnace slag, *Trans. Nonferrous Met. Soc. China*, 20(2010), No. 12, p. 2294.

[50] Y.B. Zong, D.Q. Cang, Y.P. Zhen, Y. Li, and H. Bai, Component modification of steel slag in air quenching process to improve grindability, *Trans. Nonferrous Met. Soc. China*, 19(2009), Suppl. 3, p. s834.

[51] G. Chen, J. Chen, J.H. Peng, and R.D. Wan, Green evaluation of microwave-assisted leaching process of high titanium slag on life cycle assessment, *Trans. Nonferrous Met. Soc. China*, 20(2010), Suppl. 1, p. s198.

[52] W.L. Wang, S.F. Dai, T.S. Zhang, Z.M. Li, and Y.J. Xie, Effect of isothermal and cooling rate on crystallization and viscosity of silicomanganese waste slag, *Ceram. Int.*, 47(2021), No. 10, p. 13622.

[53] J.H. Wu, F.Q. Zhang, and G.H. Chen, A new method to estimate the ability of forming amorphous solids, *Phys. Status Solidi A*, 101(1987), No. 1, p. K1.

[54] W.A. Johnson and R.F. Mehl, Reaction kinetics in processes of nucleation and growth, *Trans. AIME*, 135(1939), p. 416.